Hindawi
Journal of Engineering
Volume 2022, Article ID 4905247, 16 pages
https://doi.org/10.1155/2022/4905247

Research Article

Study on Optimization of Pump Shaft Transmission System of Plastic Centrifugal Pump

Lili Zhang, Lingfeng Tang, Qingzhao Wen, and Wenbin Luo

School of Mechanical Engineering, Anhui Polytechnic University, Wuhu 241000, China

Correspondence should be addressed to Lili Zhang; 2210120149@stu.ahpu.edu.cn

Received 27 May 2022; Revised 16 August 2022; Accepted 1 September 2022; Published 26 September 2022

Academic Editor: Ramadhansyah Putra Jaya

At present, the design of the pump shaft transmission system mostly refers to the design method of the metal pump transmission system. The dynamic and static characteristics of the plastic centrifugal pump are not related to the structural parameters of the pump shaft. Aiming at the influence of the structural parameters of the pump shaft transmission system on the dynamic and static performance of the plastic centrifugal pump, the three-dimensional model of the impeller and volute chamber was drawn by Creo5.0. The CFD calculation of the load of the plastic centrifugal pump was carried out. The flow field of the plastic centrifugal pump under ideal working conditions was simulated by ANSYS FLUENT. Combined with the application principle of singular function in mechanics, the mathematical model of a deflection of the pump shaft transmission system was constructed. Considering the minimum deflection and the maximum critical speed of the first order as the objective function, an optimization model of the structural parameters of the pump transmission system was established. The NSGA-II multiobjective optimization method was used to solve the optimal structural parameters of the optimization model, and the optimization design of the pump shaft span, cantilever, front, and rear bearing clearance was completed. The optimal span cantilever ratio of the rotor model of the single span cantilever structure was 1:0.75. Compared with the traditional design model, the optimized pump shaft deflection is reduced by 52.35%, and the first-order critical speed is increased by 42.77%. Simultaneously, using polynomial fitting as a mathematical tool, the experimental data were analyzed, and the mathematical expression of the rotation speed deflection relationship of the pump shaft at the first critical rotation speed and the corresponding function curve was obtained.

1. Introduction

Centrifugal pumps, as equipment for fluid transmission and energy conversion, are widely used in water conservancy, chemical industry, petroleum, and other industries and are also important equipment in high-tech fields such as ships, nuclear power generation, and aerospace. At present, the design method of the plastic centrifugal pump transmission system is almost completely modeled on the metal pump; that is, the minimum pump shaft diameter is designed according to the strength theory, and the corresponding structural dimensions are determined according to the structural characteristics of the pump shaft and the positioning requirements of the parts on the shaft, the span is designed according to the allowable deflection, and the stiffness is checked by using the bearing deformation. In the existing research, most scholars put forward new design ideas or improved methods for a certain part of the transmission system, without systematically expounding its design of the transmission system.

Pang et al. takes a certain axial piston pump as an example, compares the vibration acceleration and noise when water and oil are used as working media, and studies the influence of the working media on the noise and vibration of the pump [1]. By applying distributed or equivalent pulse force to different areas of the pump jet, Su et al. thinks that the response of concentrated force applied to the whole pump-jet flow field mode and excitation characteristics has a more reasonable magnitude, which shows the importance of concentrated force instead of concentrated force [2]. Li developed the pump shaft design program in the APDL language and displayed the stress distribution and the position of a dangerous section of the pump shaft under an external load through the three-dimensional model, thus

completing the design of pump shaft strength [3]. Jia et al. optimized the design and simulation of the fuel fired centrifugal pump by establishing a comprehensive loss model representing the hydraulic, volumetric, and mechanical efficiencies of impellers and volute cases [4]. Riccietti et al. improved "a new method of centrifugal pump parametric design suitable for a wide range of specific speed" and also included the use of a support vector machine as a classification tool. The addition of this classification tool can significantly reduce the number of CFD calculations required for centrifugal pump design and save a lot of calculation time [5]. Wu et al. puts forward a design method of the centrifugal pump impeller combining the manufacturing process with numerical simulation, which can manufacture centrifugal impellers with good flow field characteristics [6]. Khor et al. used finite element software to analyze the structure of pump casings with different thicknesses and studied the correlation between wall thickness and mechanical properties. It was found that, with the increase in wall thickness, the mechanical properties of the pump casings were improved [7]. To realize the multiobjective optimization of pump efficiency and cavitation performance, Xu et al. adopted the orthogonal design method, established an impeller orthogonal design table and found an efficient and low-cost optimization method for the centrifugal pump [8]. Rajmane and Kallurkar believed that the physical structure of the pump was the factor that affects the pump operation and used CFD technology to study the previous and modified configurations, in which the optimal configuration was found [9]. According to the Bayesian framework, Zhang et al. constructed a centrifugal pump hydraulic design method based on the multi-output Gaussian process regression (MOGPR) model and used it to design the hydraulic design of the M125-100 centrifugal pump impeller, which improved the efficiency and head of the pump and reduced the turbulent kinetic energy [10].

In this study, the plastic centrifugal pump shaft is taken as the research object, the three-dimensional model of the impeller and volute chamber is drawn by Creo5.0, and the mathematical model of the deflection of the plastic centrifugal pump shaft is deduced based on the application principle of singular function in mechanics, and the radial force and axial force on the pump shaft are calculated theoretically. Based on the ANSYS FLUENT software, the flow field of the plastic centrifugal pump under ideal working conditions is simulated, and the key factors affecting the deflection of the pump shaft are analyzed. The ZT-3 rotor test device is used as a platform to verify the influence of the ratio of span to cantilever on the dynamic performance of the rotor.

2. Methods

In this study, the pump shaft of a plastic centrifugal pump is taken as the research object. The material of the pump shaft is 45# steel, which needs to be quenched and tempered. The allowable shear stress is determined to be 45 MPa by consulting the mechanical engineering materials manual.

2.1. Theoretical Calculation of Pump Shaft Load of Plastic Centrifugal Pump. It is of great significance to determine the type, size, and position of the external load to analyze the stress of the pump shaft system. In a static state, the dead weight of the plastic centrifugal pump is the main external load of the pump shaft. When the centrifugal pump is dynamic, the force generated by the flow field will be superimposed on the pump shaft, and the analysis of its force will be more real and effective.

The axial force produced by the centrifugal pump is the main inducement of axial displacement of the pump shaft transmission system, and the radial force is the main reason for the directional deflection and alternating stress of the pump shaft[11].

2.1.1. Axial Force Analysis. According to [12], the axial force generated by the pump during operation can be obtained, which is the force generated by the asymmetry of the front and rear cover plates of the impeller and the force caused by the difference between the suction pressure at the shaft end and the atmospheric pressure. It will push the pump shaft to move in the axial direction so that the speed of the liquid will change from the axial direction to the radial dynamic reaction force after the liquid enters the impeller:

$$T_1 = R_2^2 - R_h^2\pi\rho g H_p - \frac{1}{2}R_2^2 - R_h^2\pi\rho g\frac{\omega^2}{8g}R_2^2 - R_h^2 - \frac{1}{2}H_p\rho g\left(R_2 - R_m\right)2\pi\left[R_m + \frac{2}{3}\left(R_2 - R_m\right)\right], \tag{1}$$

where R_2 is the impeller outlet radius, R_h is the effective hub radius of the impeller, H_p is the potential outlet lift, ω is the rotational angular velocity of the impeller, and R_m is the radius of the impeller sealing ring.

The reaction force T_2 is calculated according to:

$$T_2 = \rho Q_t\left(v_{m0} - v_{m3}\cos\alpha\right), \tag{2}$$

where ρ is the fluid density, Q_t is the theoretical flow rate of a plastic centrifugal pump, v_{m0} is the axial velocity slightly before the blade inlet, v_{m3} is the axial velocity of the blade outlet later, and α is the angle between the impeller outlet axial velocity and the axial direction, $\alpha = {}^{0^\circ}$.

The axial force T_3 caused by cantilever impeller shaft head structure was calculated according to the formula (3). Since the inlet pressure is negative and less than atmospheric pressure, the direction of the force is opposite to T_1:

$$T_3 = \frac{d_t^2}{4}\pi\left(p_1 - p_a\right), \tag{3}$$

where p_1 is the inlet pressure of the centrifugal pump, p_a is the atmospheric pressure, and d_t is the shaft diameter at the packing.

The approximate calculation of the axial force is calculated according to:

$$T = T_1 + T_2 + T_3 = H_1 k_4\rho g\pi\left(R_m^2 - R_h^2\right), \tag{4}$$

where T is the total axial force, H_1 is the single-stage lift of a plastic centrifugal pump, and k_4 is the coefficient, $k_4 = 0.6$.

2.1.2. Radial Force Analysis. The reason why the plastic centrifugal pump generates radial force during the operation is that when the actual flow rate of the screw press water chamber is different from the design flow rate, the pressure in it is no longer symmetrically distributed along the impeller axis. Instead, it acts directly on the impeller to form a radial force, causing the pump shaft to form directional deflections and vibrations when it rotates. In addition, the dynamic reaction force of the liquid flowing out of the impeller is also the main reason for the radial force of the impeller.

The radial force of the plastic centrifugal pump is composed of the dead weight of the impeller, the hydraulic radial force of the impeller, and the centrifugal force of the unbalanced mass [13]. The excessive radial force will cause the vibration of the centrifugal pump and increase the deflection of the pump shaft, destroy the stability of the pump shaft, aggravate the wear of rubber seals and shaft sleeves, lead to shaft seal leakage, and even increase the risk of fatigue fracture of the pump shaft.

(1) Three-Dimensional Modeling and Dead Weight Calculation of Overcurrent Components. The basic design parameters of the plastic centrifugal pump are shown in Table 1.

The basic design parameters of centrifugal pump structure parameters is shown in Tables 2 and 3.

According to the aforementioned parameters, Creo5.0 is used to model the flow-through parts, and the results are shown in Figures 1 and 2.

ABS was selected as the impeller material, and its density was $1.1 \times 10^3\,\mathrm{kg/m^3}$. According to the three-dimensional model, the self-weight of the impeller, $m = 0.62\,\mathrm{kg}$, can be directly obtained, that is, $G = mg = 6.13\,\mathrm{N}$.

(2) Calculation of Hydraulic Radial Force of the Impeller. In this project, the radial force caused by the centrifugal pump working at nonrated flow is called the hydraulic radial force of the impeller. The test proves that the hydraulic radial force, Fr, changes smoothly under the rated flow condition, and Fr transforms greatly under the nonrated flow condition. The maximum peak value can reach 5~10 times the weight of the impeller [6], that is, $F_1 = (5\sim10)\,G = 30.38\sim60.76\,\mathrm{N}$, take $F_1 = 50\,\mathrm{N}$.

(3) Centrifugal Force Calculation of Unbalanced Mass. Stepanoff calculated the centrifugal force of the unbalanced mass according to the measured data, and he proposed to calculate the stable radial force according to [7]

$$F_2 = K_r \rho g H D_2 b_2, \tag{5}$$

where H is the head of the plastic centrifugal pump and K_r is an experimental coefficient, calculated according to:

Table 1: Basic design parameters of the plastic centrifugal pump.

Parameter	Traffic: Q (m^3/h)	Lift: H (m)	Speed: n (r/min)
Value	50	13.3	1450

Table 2: Each plastic centrifugal pump structure parameters.

Parameter	Values
Import diameter of the pump: D_S (mm)	80
Import flow velocity of the pump: v_s (m/s)	2.76
Outlet diameter of the pump: D_d (mm)	72
Export flow velocity of the pump: v_d (m/s)	3.41
The specific speed of the pump: n_s	89.56
The efficiency of the pump: η	0.74
The power of the pump: P (kW)	2.46
The power of driving motor: P_c (kW)	2.96
The output torque of motor: M_n (N·m)	19.47
The minimum diameter of pump shaft: d (mm)	20
The diameter of the wheel hub: d_h (mm)	60
Import diameter of the impeller: D_1 (mm)	85
Outlet diameter of the impeller: D_2 (mm)	210
Outlet width of blade: b_2 (mm)	15
Inlet placement angle of blade: β_1 (°)	19
Outlet mounting angle of blade: β_2 (°)	33
Number of leaves: z_y	6
Blade wrap angle: φ (°)	123
Inlet thickness of blade (mm)	4
Outlet thickness of blade (mm)	8
Diameter of base circle of volute section: D_s (mm)	210
Inlet width of volute: b_3 (mm)	25
Placement angle of septum tongue: φ_0 (°)	22
Taper of suction chamber: (°)	15
Length of conical tube: (mm)	200

$$K_r = 0.36\left[1 - \left(\frac{Q}{Q_N}\right)^2\right], \tag{6}$$

$$F_2 = 106.25\,\mathrm{N}.$$

The formula is related to a specific speed, and it is considered that the calculation is more accurate when $n_s > 165$.

From the above analysis, the traditional axial force and radial force are calculated by an empirical formula, and the establishment of an empirical formula often needs certain assumptions or boundary conditions, so it cannot fully reflect the change process of force.

2.2. CFD Calculation of Plastic Centrifugal Pump Load. Based on the fluid continuity equation, Navier–Stokes equation, and turbulent mode theory, CFD [9, 14] is used to simulate the flow field of a plastic centrifugal pump. Since the material is water at room temperature, the incompressible fluid continuity equation is chosen. From the perspective of momentum, I analyze the force generated by the fluid microelement moving in a certain direction, which is the sum of the fluid surface force and the volume force in this direction, and deduce the Navier–Stokes equation in the right-hand Cartesian coordinate system. I assume that the

Table 3: Sectional area of cochlear chamber.

Section number	1	2	3	4	5	6	7	8
Sectional wrap angle: φ_0	45	90	135	180	225	270	315	360
Area: F_i	246.11	492.22	738.34	984.45	1230.56	1476.67	1722.78	1968.90

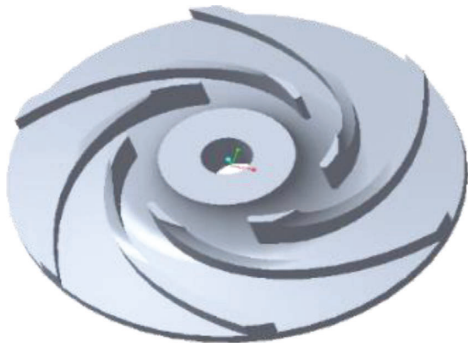

Figure 1: Three-dimensional view of the impeller.

Figure 2: Three-dimensional view of the cochlear chamber.

flow field of the plastic centrifugal pump is completely turbulent and ignores the influence of molecular viscosity on the fluid flow, so I choose the standard k-ε model. The diffusion equation ε of turbulent kinetic energy is considered on the equation of turbulent kinetic energy k, and default coefficients are chosen when setting up the standard k-ε model.

2.2.1. Simulation Calculation Based on ANSYS Fluent. The simulation process of ANSYS Fluent software mainly includes the following steps: creating geometry, dividing mesh, adding boundary, solving equation, and analyzing result [15].

(1) Create Geometry. In this study, the cantilever single-stage plastic centrifugal pump is taken as the research object, and the hydraulic components that meet the technical parameters are designed to provide a practical and reliable physical model for the stress analysis of the pump shaft. Y2–132S1-2-4 kW motor is selected, the blade line type is equal variable angle logarithmic spiral line type, the water pressure chamber is of a single volute structure, the volute section shape is pear-shaped, and the water suction chamber is of cantilever conical tube structure. According to the parameters in Tables 2 and 3, the hydraulic model of impeller and volute is drawn with Creo5.0, and the structure is shown in Figures 3 and 4.

(2) Mesh. ANSYS14.0 ICEM is used to divide the above two models into unstructured meshes, and the division results are shown in Figures 5 and 6. The grid number of the impeller hydraulic model is 69835, the grid quality is 0.23, the grid number of the volute hydraulic model is 431019, and the grid quality is 0.16. The two models are merged into the hydraulic model grid of the plastic centrifugal pump, and the post-processing is output by ANSYS Fluent; the result is shown in Figure 7.

(3) Add Boundary. The mesh file is imported into FLUENT to set the boundary conditions of the model. The inlet conditions of the plastic centrifugal pump adopt velocity inlet, the inlet water velocity is set to 2.76 m/s, the outlet is set to outflow, and the rest are set to default.

(4) Solve Equation. The algorithm adopts the SIMPLE mode, and a standard initialization is used. According to the hydraulic design of the centrifugal pump, the initial water velocity is 2.76 m/s and the inlet diameter is 80 mm. The Reynolds coefficient of the centrifugal pump inlet is $R_e = (vD_s/V)$, turbulence intensity is $I_k = 0.16 \times R_e^{-1/8}$, turbulence kinetic energy is $k = 1.5 \times (v \times I_k)^2$, and the turbulence dissipation rate is $\varepsilon = C_u^{3/4} \times (k^{3/2}/l_1)$, where v is mean velocity, D_s is the hydraulic diameter, V is hydraulic diameter, the kinematic viscosity of water is 1.00481×10^6, Cu is coefficient, usually $Cu = 0.09$, and l_1 is the turbulence length scale, $l_1 = 0.07D_s$.

After calculation, $R_e = 2197433.3$, $I_k = 0.025785795$, $k = 0.007597496$, and $\varepsilon = 0.00194312$, enter the above parameters into the initial condition setting dialog box.

The residual option is set to 10^{-3}, the number of iterations is proposed to be 3000, and the simulation process converges at 587 steps of iteration, as shown in Figure 8.

2.3. Construction and Experimental Method of Test Bed. This experiment is to analyze the influence of different spans and cantilever ratios on the radial vibration of the rotor-bearing system under the same load, with the cantilever single span rotor test bed as the platform and rotor dynamics as the theoretical basis.

The ZT-3 vibration test bed consists of a vibration test-bed, DH5910A data acquisition function recorder, an eddy current sensor, a photoelectric sensor, and signal test and analysis system software. The test bed is of modular

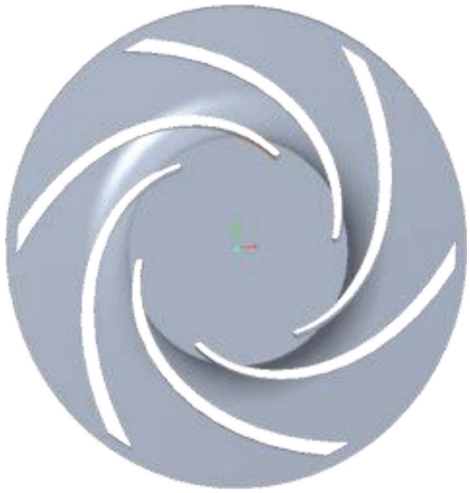

Figure 3: Hydraulic model of the blade.

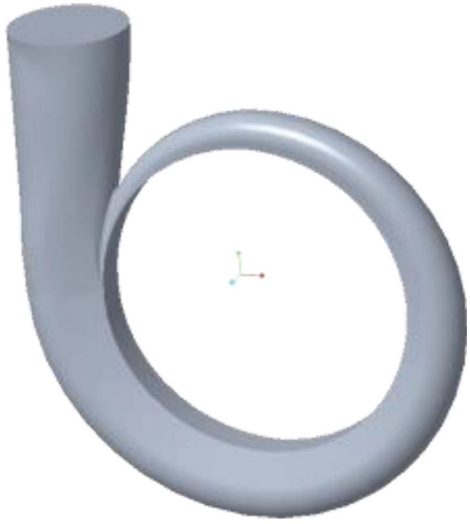

Figure 4: Volute hydraulic model.

Figure 5: Hydraulic grid of the impeller.

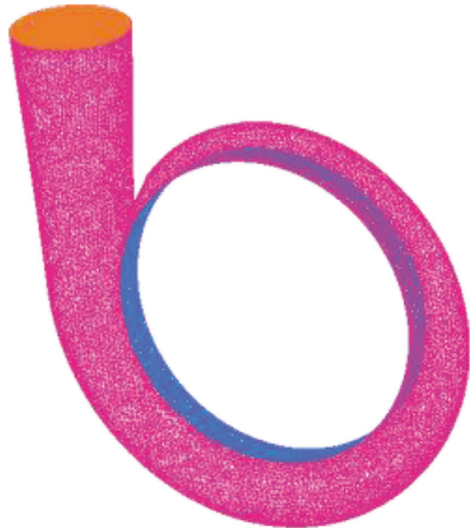

Figure 6: Hydraulic grid of the volute.

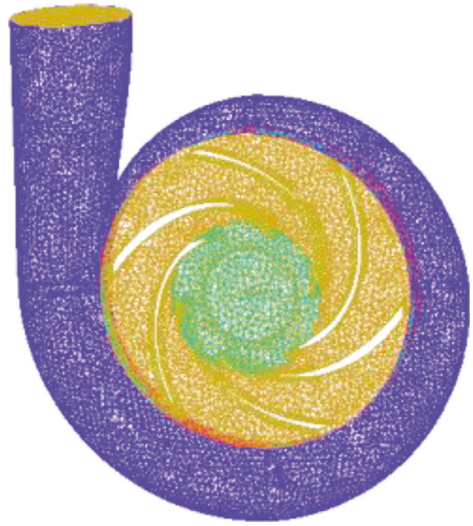

Figure 7: Hydraulic grid of the plastic centrifugal pump.

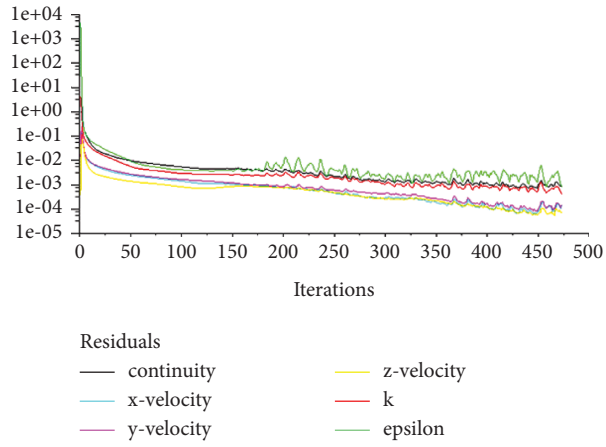

Figure 8: Residual curve of the plastic centrifugal pump.

structure, and the structure, span, and rotor quality of the shafting can be adjusted and changed, and it can effectively simulate the common faults of the rotor system such as unbalance, misalignment, and rubbing. The test bed is of modular structure, and the structure, span, and rotor quality of the shafting can be adjusted and changed, and it can effectively simulate the common faults of the rotor system such as unbalance, misalignment, and rubbing. The test bench is shown in Figure 9 and the physical drawing is shown in Figure 10. The test bed is a comprehensive test bed, which consists of a DC motor, disc rotor, and a speed control system. The displacement, velocity, acceleration, and other detection sensors can be flexibly installed within the scope of the bench for comprehensive engineering measurement. See Table 4, for the technical parameters of each bench component.

The data acquisition system DH5910A of the test bed is adopted, and the frequency range of the system is from 10 Hz to 128 Hz, which can meet most types of measurement requirements. The eddy current displacement sensor and photoelectric speed sensor are used in the test bed. The model of the eddy current sensor used in the test bed is HZ-891YT08HP-M10×1-B-01-05-50. The test bed uses a photoelectric speed sensor to measure the rotating speed of the transmission shaft, which is a reflective photoelectric sensor.

The test bed is driven by a DC motor and connected to a rotating shaft through a rigid coupling, and then, the rotating shaft drives the disk rotor to rotate. The rotational speed of the system is acquired by the photoelectric rotational speed sensor, and the vibration displacement of the system is collected by the eddy current sensor. The signal is filtered and shaped by the collector and connected to the monitoring computer through the 1394 card. The structure is shown in Figure 11. According to the structure of the pump shaft of the plastic centrifugal pump, adjust the test bed to a single span cantilever structure, as shown in Figure 12.

Because of the structural form and installation error of the rotor, the rotor will inevitably cause vibration in the rotating operation. Its differential equation of motion is shown in equation (7), so the amplitude and phase angle of the system is shown in equations (8) and (9), which can be easily obtained. The vibration of the rotor is related to its rotation frequency, and the phase difference remains unchanged:

$$\ddot{x} + 2\xi\omega_n\dot{x} + \omega_n^2 x = e\omega_1^2 e^{i\omega_1 t}, \tag{7}$$

$$|A| = \frac{e\left(\omega_1/\omega_n\right)^2}{\sqrt{\left[1-\left(\omega_1/\omega_n\right)^2\right] + \left(2\xi\omega_1/\omega_n\right)^2}}, \tag{8}$$

$$\tan\varphi = \frac{2\xi\left(\omega_1/\omega_n\right)}{1-\left(\omega_1/\omega_n\right)^2}. \tag{9}$$

The test stand determines the fixed phase φ by the reflective label marked on the coupling, as shown in Figure 13. Although the value range of φ is a positive value within 0~360, it always lags behind the fixed phase. In order to accurately measure the phase, four points Q_1~Q_4 can be set on the rotating shaft. When the Q_1 point turns to the measuring position of the photoelectric sensor, the signal generated by vibration happens to be at the positive peak point, which is called the positive peak point phase. Similarly, Q_2 is the negative slope zero-crossing phase, Q_3 is the negative peak phase, and Q_4 is the positive slope zero-crossing phase. The principle is shown in Figure 14. ZT-3 test bed system adopts a positive peak-point phase measurement method.

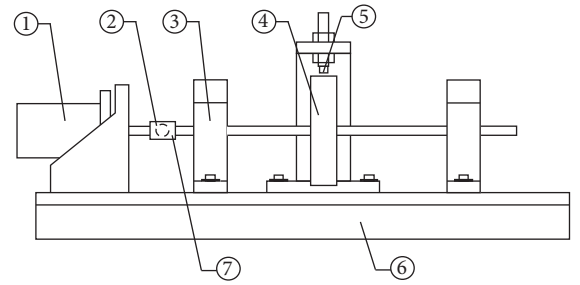

1. Electrical machinery 2. Photosensor 3. Bearing chock 4. Disk rotor 5. Eddy current sensor 6. Base 7. coupling

Figure 9: ZT-3 multifunction rotor simulation test bench.

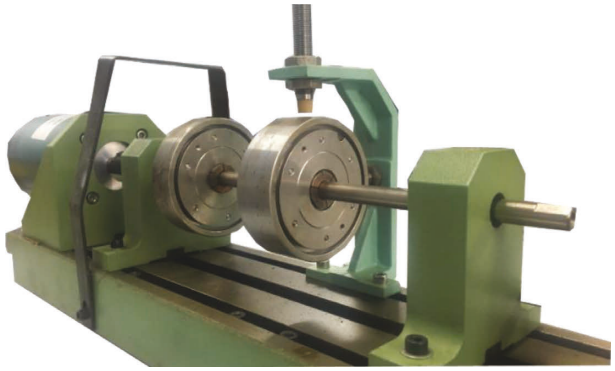

Figure 10: ZT-3 rotor test stand.

Hardware is connected according to Figure 15. Among them, it is necessary to ensure that the gap between the probe of the eddy current sensor and the measured surface of the transmission shaft is between 0.98 and 2.98 mm and 2.98 mm so that the sensor can easily collect the vibration displacement signal of the rotating shaft. The parameter settings of the software are shown in Table 5.

The layout of the measuring points of the test bed is shown in Figure 16. The experiment is designed into three groups, namely, the span cantilever ratio is 1 : 1 (in traditional design, the span and overhang of the pump shaft are usually equal), 1 : 0.75 (the best result above is that the span is 156 mm, the overhang is 118 mm, and the ratio is about 0.75), and 0.8 : 1.

3. Results and Discussion

3.1. Results of Theoretical Calculation of Pump Shaft Load. The axial force of a plastic centrifugal pump consists of cover force, an axial force caused by the axial structure, and

Table 4: Technical parameters of test bench components.

Part name	Parameter name	Value
Test bed base	Length × width × height	1200 mm × 108 mm × 145 mm
	Weight	45 kg
Axle	Diameter of axle	9.5 mm
Speed controller	Rated current	2 A
	Maximum output power	250 W
	Speed adjustable range	0~10000 rpm
Disk rotor	Measure	Φ76 × 25 mm and Φ76 × 19 mm
	Weight	800g and 600 g

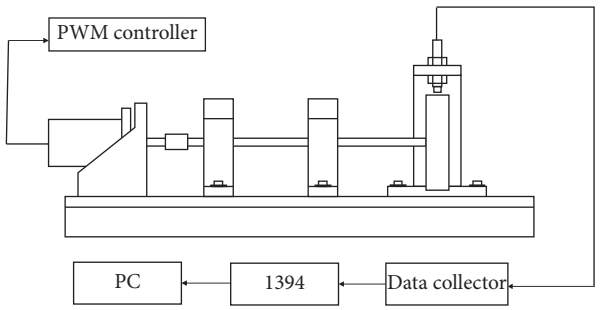

Figure 11: Test bench test system connection diagram.

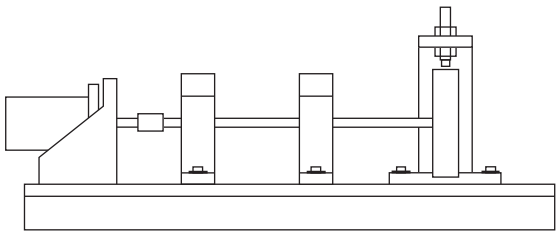

Figure 12: Simulate the pump shaft structure of the plastic centrifugal pump on test stand.

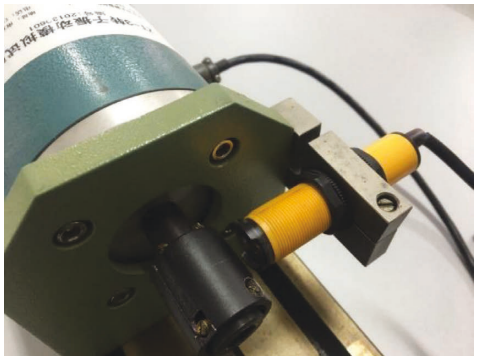

Figure 13: Rotating speed photoelectric encoder of test stand.

reaction force, calculated by formulas (1)~(4) can be obtained from the axial force:

$$T = 582.31\,\text{N}. \tag{10}$$

The radial force of the plastic centrifugal pump is composed of the impeller dead weight, the hydraulic radial force of the impeller, and the centrifugal force of the unbalanced mass. The radial force can be calculated from the 3D modeling results and formulas (5) and (6):

$$F = 162.38\,\text{N}. \tag{11}$$

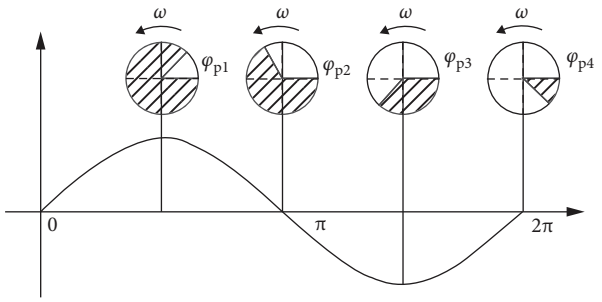

Figure 14: Four phase angles define corresponding positions.

3.2. Result of Simulation Calculation Based on ANSYS FLUENT

3.2.1. Analysis of Internal Flow Field Simulation Results. Figure 17 shows the pressure cloud chart of the plastic centrifugal pump under the standard working condition flow rate. It can be seen from the chart that the negative pressure at the inlet facilitates the suction of clean water, which is consistent with the actual situation. However, the pressure distribution of the liquid in the flow field is uneven, especially the pressure loss that increases at the eighth to eleventh sections of the volute chamber, which destroys the balance of the impeller and easily causes the vibration of the centrifugal pump.

From Figure 18, it can be seen that the velocity of the fluid at the septum of the cochlear chamber is disordered, that is, the phenomenon of fluid impact appears, accompanied by the backflow and vortex of the liquid. However, it can be seen that the impact is not very obvious, which can be confirmed by the turbulent kinetic energy distribution cloud chart in Figure 19.

3.2.2. Simulation Results of Axial Force and Radial Force. The radial force and axial force of the flow field of a plastic centrifugal pump analyzed by ANSYS FLUENT software are shown in Tables 6 and 7.

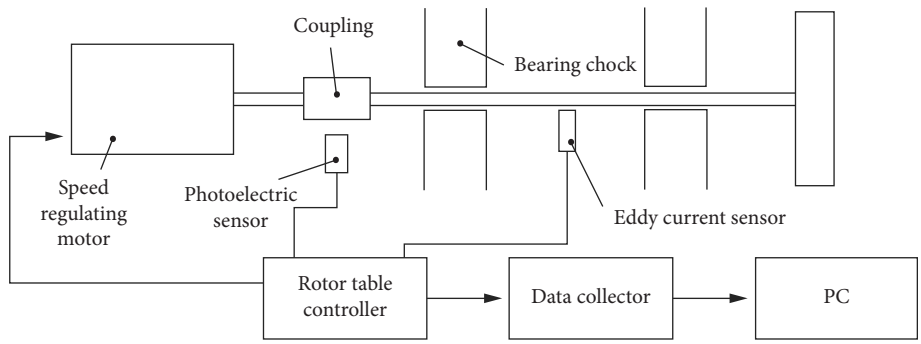

Figure 15: Test system composition diagram.

Table 5: Software parameter settings.

Parameter name	Value
Spectral line number	4
Service aisle	8
Input mode	AC
Value type	Peak
End speed	5000 r/min
Secondary upper limit	8

It can be seen from Tables 6 and 7 that the radial force $F_r' = 116.11$ N and the axial force $F_t' = 324.21$ N of the plastic centrifugal pump. However, the radial force in Table 6 is calculated without considering the dead weight of the overcurrent component, so the final radial force calculation is corrected according to:

$$F_r = mg + F_r', \tag{12}$$

where F_r' is comprehensive radial force calculated by CFD:

$$F_r = 6.13 + 116.11 = 122.24\,\text{N}. \tag{13}$$

3.2.3. Analysis of Independence of Grid Division. In this study, the hydraulic models of the impeller and volute chamber are all irregular parts, so an unstructured grid division is adopted. The initial parameters of the grid are set with the global grid-scale factor, the maximum size in the control model, and the number of refinement layers in the boundary layer as indicators and the number and quality of grids as the evaluation criteria. Taking the impeller grid division as an example, the initial parameters and results of each group are shown in Table 8.

Analysis of Table 8 shows that the number and quality of the fourth to sixth groups of divided grids are better. Therefore, the above three groups of results are combined with the hydraulic grid of the same volute chamber and brought into FLUENT software to simulate separately. The boundary conditions of each group are set to be consistent. The simulation results of the axial force and radial force of each group are shown in Table 9.

It can be seen from Tables 8 and 9 that, under the same grid quality condition, when the boundary grid size is larger and the number of layers is smaller, the overall grid number is smaller and the calculation speed is faster, but the result deviation is larger, such as in the fifth group of data. However, when the boundary grid size is small and the number of layers is large, the total number of grids is huge and the calculation is slow, but the results are closer to the true value, such as the sixth group of data.

To sum up, the number of grids has a certain influence on the simulation results, but the influence on the results will no longer be obvious when the number exceeds a certain threshold; that is, the calculation results have nothing to do with the degree of grid division, and the number of grids at this time is relatively reasonable.

3.3. Design and Optimization of Pump Shaft Transmission System of the Plastic Centrifugal Pump. The transmission system of the plastic centrifugal pump consists of the pump shaft, rolling bearing, rigid coupling, and mechanical shaft seal, among which the bearing, coupling, and shaft seal are all standard parts, which can be selected in the design. The pump shaft is the core part of the design and optimization of the transmission system of the plastic centrifugal pump.

3.3.1. Deflection Analysis of Pump Shaft of the Plastic Centrifugal Pump. The single-span overhanging structure is a widely used design form of single-stage centrifugal pump shafting, as shown in Figure 20. Because the impeller is located at the free end of the shaft extension, the pump shaft will be bent and deformed by the self-weight and load of the impeller, and simultaneously, the dynamic reaction force of the bearing will increase, which will damage the motion state of the bearing. Deflection is used as an index to measure the deformation degree of a pump shaft in engineering.

In classical mechanics, it is necessary to establish the bending moment equation in sections for the deflection equation of the stepped shaft, and each section needs to be integrated twice to obtain the rotation angle and deflection equation, and then, the results are brought to the next section for calculation, and the whole process is tedious and lengthy. The singular function can just overcome the problems in classical mechanics. The whole shaft needs only a one moment equation to express it. Secondly, the singular function also has excellent calculus characteristics, which can quickly find out the rotation angle and deflection equation of the shaft and greatly reduce the calculation amount.

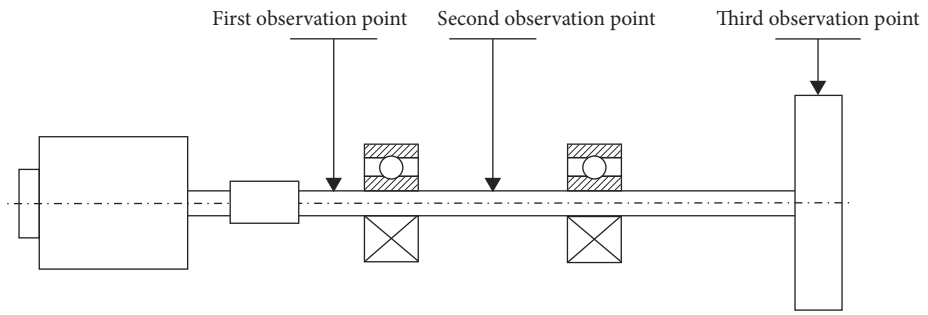

Figure 16: Distribution of test points on test stand.

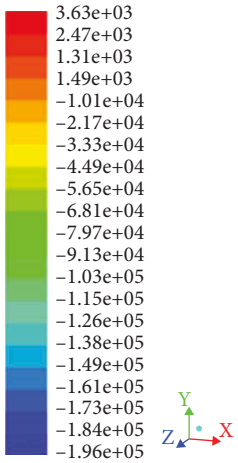

Figure 17: Nephogram of pressure distribution of plastic centrifugal pump.

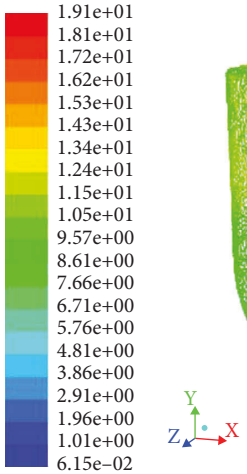

Figure 18: Isogram of velocity distribution of the plastic centrifugal pump.

(1) Singular Function Model of Pump Shaft Deflection. The differential equation of pump shaft deflection is shown as

$$Ey'' = \frac{M(x)}{I(x)}, \tag{14}$$

where E is the elastic modulus of the pump shaft material, $M(x)$ is the bending moment of the shaft under load, $I(x)$ is the moment of inertia of the pump shaft, and "y''" is the pump shaft deflection.

In order to meet the requirements of design strength and lightweight, the pump shaft is usually designed as a stepped

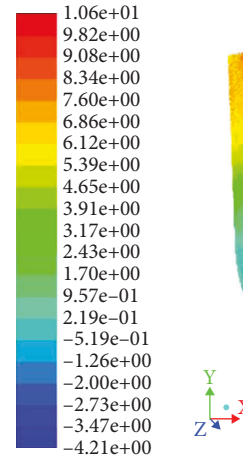

Figure 19: Turbulent kinetic energy stress nephogram.

Table 6: Summary of radial force of the plastic centrifugal pump.

CFD calculation area	Pressure	Stickiness	Radial force
Wall-3	76.602567	0.10087125	76.703439
Wall-4	−130.7379	−0.16132757	−130.89923
Woke_wall	60.542046	8.9448017	69.486848
Gaiban	24.058556	−2.501077	21.577479
Yepian	−151.65696	−1.3029632	−152.95992
Sum	−121.19169	5.0803044	−116.11138

Table 7: Summary of axial force of the plastic centrifugal pump.

CFD calculation area	Pressure	Stickiness	Radial force
Wall-3	−0.087881957	0.0040318954	−0.083850062
Wall-4	−0.0021913949	0.21142651	0.20923511
Woke_wall	−4.1930287	−0.46356282	−4.6565915
Gaiban	331.84718	−1.3708198	330.47636
Yepian	0.52347127	−2.2585918	−1.7351206
Sum	328.08755	−3.8775161	324.21003

Table 8: Results of impeller grid division.

Name	First group	Second group	Third group	Fourth group	Fifth group	Sixth group
Global grid-scale factor	2	2	1	1	1	1
Control the maximum size of the model	2	1	4	8	8	8
Layer number of boundary layer refinement	5	5	5	5	2	10
Grid quality	0.15	0.2	0.23	0.23	0.23	0.25
Grid quantity	133565	984290	133527	69835	44149	125397

Table 9: Simulation results of axial force and radial force of each group.

Group	Axial force (N)	Radial force (N)
Fourth group	324.21003	116.11138
Fifth group	230.01891	84.99353
Sixth group	341.06895	121.91695

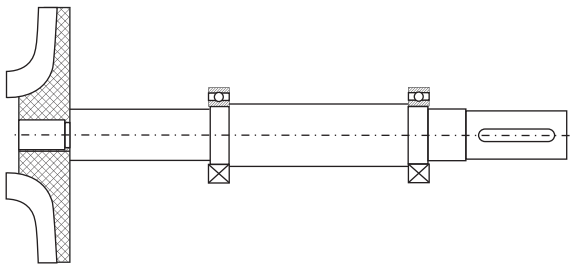

Figure 20: Structure diagram of the pump shaft system.

shaft. According to the different diameters, the shaft is divided into n sections; then, the inertia moments of each section are $I_1, I_2, I_3, \ldots, I_i, \ldots, I_n$. Using the step function in the singular function, the reciprocal of the inertia moments of the step shaft of N sections can be expressed as

$$\frac{1}{I(x)} = \sum_{1}^{n} \beta_i \langle x - x_{i-1} \rangle^0, \tag{15}$$

where

$$\begin{aligned} \beta_i &= \frac{1}{I_i} - \frac{1}{I_{i-1}}, \\ x_0 &= 0, \\ \frac{1}{I_0} &= 0. \end{aligned} \tag{16}$$

(2) Solution of Pump Shaft Deflection

(a) Solution of Bending Moment Equation $M(x)$

In classical mechanics, it is necessary to establish the bending moment. The shafting structure of the plastic centrifugal pump is shown in Figure 20, and the size of the pump shaft is shown in Figure 21. Assuming that the total length of the pump shaft is L, its mechanical model can be simplified, as shown in Figure 22.

According to the stress analysis, it is found that the relationship between the concentration q of the outer line distribution, shear force $Q(x)$, and bending moment $M(x)$ is shown as

$$\begin{cases} Q(x) = -q\left[x - 0^1 - x - \frac{1}{12}L^1\right] \\ \qquad + R_A x - \frac{19}{52}L^0 + R_B x - \frac{8}{11}L^0 \\ M(x) = -\frac{q}{2}\left[x - 0^2 - x - \frac{1}{12}L\right]^2 \\ \qquad + R_A x - \frac{19}{52}L^1 + R_B x - \frac{8}{11}L^1 \end{cases}. \tag{17}$$

(b) Solution of Moment of Inertia $I(x)$

The pump shaft consists of 8 sections, and a coordinate system is created with the center of the left end face as the zero point. The position of the length of each section of the shaft in the coordinate system is shown in Figure 23. If $I = I_1$, the β value of each section of the pump shaft can be calculated according to formula (18), and the results are shown in Table 10.

Bring the parameters in Table 10 into formula (15) to get the reciprocal of the total section moment of inertia of the pump shaft, then bring formula (17) and the reciprocal of the solved total section moment of inertia into formula (14) and integrate the results once to get the angle equation $\theta(x)$, such as

$$\begin{aligned} \theta(x) = \frac{1}{EI}\Bigg[& -\frac{q}{6}\left[\langle x-0\rangle^3 - \langle x - \frac{1}{12}L\rangle^3\right] \\ & + \frac{R_A}{2}\langle x - \frac{19}{52}L\rangle^2 + \frac{R_B}{2}\langle x - \frac{8}{11}L\rangle^2\Bigg] \\ & \Bigg[1 + \frac{49}{34}\langle x - \frac{L}{12}\rangle^1 - \frac{103}{45}\langle x - \frac{9}{97}L\rangle^1 \\ & - \frac{2}{35}\langle x - \frac{8}{23}L\rangle^1 - \frac{2}{73}\langle x - \frac{18}{47}L\rangle^1 \\ \times + & \frac{2}{73}\langle x - \frac{22}{31}L\rangle^1 + \frac{2}{35}\langle x - \frac{35}{47}L\rangle^1 + \frac{1}{29}\langle x - \frac{79}{97}L\rangle^1 \%\Bigg] \\ & + \frac{17 - 7L}{17EI}\left(\frac{q}{94}L^3 - \frac{23R_A}{1404}L^2 - \frac{23R_B}{1046}L^2\right). \end{aligned} \tag{18}$$

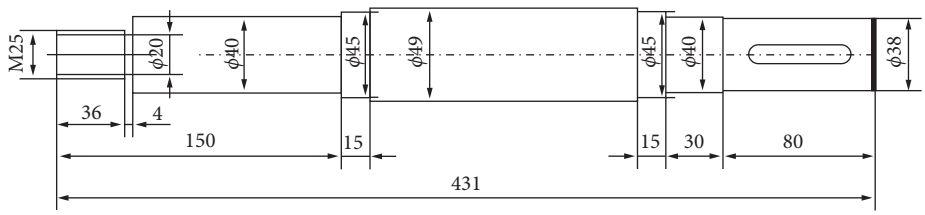

Figure 21: Dimension drawing of the pump shaft.

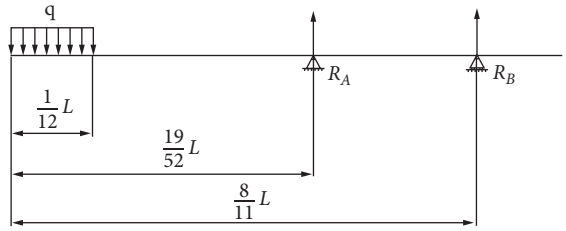

Figure 22: Mechanical diagram of the pump shaft.

The deflection curve equation $y(x)$ can be obtained by integrating the angle equation $\theta(x)$ again:

$$\begin{aligned} y(x) = {} & \frac{1}{EI}\left[-\frac{q}{24}\left[\langle x-0\rangle^4 - \langle x-\frac{1}{12}L\rangle^4\right]\right. \\ & + \frac{R_A}{6}\langle x-\frac{19}{52}L\rangle^3 + \frac{R_B}{6}\langle x-\frac{8}{11}L\rangle^3\%] \\ & \times\left[1 + \frac{49}{68}\langle x-\frac{L}{12}\rangle^2 - \frac{103}{90}\langle x-\frac{9}{97}L\rangle^2\right. \\ & - \frac{2}{70}\langle x-\frac{8}{23}L\rangle^2 - \frac{2}{146}\langle x-\frac{18}{47}L\rangle^2 \\ & + \frac{2}{146}\langle x-\frac{22}{31}L\rangle^2 + \frac{2}{70}\langle x-\frac{35}{47}L\rangle^2 + \frac{1}{58}\langle x-\frac{79}{97}L\rangle^2\%] \\ & + \frac{17-7L}{17EI}\left(\frac{q}{94}L^3 - \frac{23R_A}{1404}L^2 - \frac{23R_B}{1046}L^2\right)x \\ & + \frac{q}{EI}\left(\frac{2}{118233}L^6 - \frac{4}{823}L^4 + \frac{1}{94}L^3\right) \\ & + \frac{R_A}{EI}\left(\frac{161}{23868}L^3 - \frac{23}{1404}L^2\right) \\ & + \frac{R_B}{EI}\left(\frac{80}{286749}L^5 - \frac{1}{860}L^3 - \frac{23}{1406}L^2\right). \end{aligned} \quad (19)$$

3.3.2. Establishment of the Pump Shaft System Optimization Model. Stiffness is the ability of a material or structure to resist elastic deformation when stressed. When the external load is a static force, the ability of an object to resist deformation is called static stiffness, which changes with the position and direction of the load. The static stiffness of the pump is described by the ratio of the static load P applied to the shaft end to the deformation Y generated along the load direction, that is,

$$K = \frac{P}{y}, \quad (20)$$

where P is static load or static torque and y is the deformation, displacement, or torsion angle.

The essence of optimizing the static stiffness of the pump is to reduce the deflection of the shaft. According to formula (19), there are two ways to increase the static stiffness of the pump shaft: one is to reduce the external load; the second is to change the structural size of the pump shaft. The external load of the shaft consists of the dead weight of the plastic centrifugal pump and the radial force and axial force generated when working, and its magnitude cannot be changed.

The cantilever length of the pump shaft is usually designed by the empirical method; that is, the cantilever length is equal to the span. It can be seen from formula (19) that the relationship between the overhang of the pump shaft and the deflection is cubic. When the overhang changes within the design value range, the influence on the deflection value is shown in Figure 24. When the optimization space of the overhang is larger, the deflection of the pump shaft will change significantly.

Clearance is the relative movement of the inner and outer rings of the bearing. Axial clearance can be controlled by the selection of bearing parts and the adjustment of radial clearance, so the adjustment of pump shaft bearing clearance refers to the adjustment of radial clearance. In this study, 6009CE deep groove ball bearings are selected for the design. According to the relevant parameters in GB/T4604-2006 and related calculations, it can be determined that the installation clearance $\Delta_A = 34.08\,\mu$m, the working clearance $\Delta_r = 3.855\,\mu$m, the variation of the bearing clearance caused by temperature $\delta_t = 17.6\,\mu$m, and the variation of the bearing clearance caused by the working load $\delta_w = 1.144\,\mu$m. To sum up, the calculated original clearance of the bearing is $\Delta_0' = \Delta_r + \Delta_A + \delta_t - \delta_w = 3.855 + 34.08 + 17.6 - 1.144 = 54.391\,\mu$m. Select the C4 group of deep groove ball bearings according to GB/T 4604–2006, and the radial clearance range of the bearing can be obtained, $\Delta_{0\min} = 30\,\mu$m and $\Delta_{0\max} = 51\,\mu$m, so the clearance range of the bearing is [−24.39, −3.39].

The pump shaft is the power transmission component of a centrifugal pump, and its dynamic and static characteristics are mainly manifested in three aspects: rotation accuracy, vibration resistance, and static stiffness, among which static stiffness is the foundation of the latter two, and static stiffness is guaranteed by the structural parameters of the pump shaft, so it is very necessary to optimize the multiobjective structure of the pump shaft.

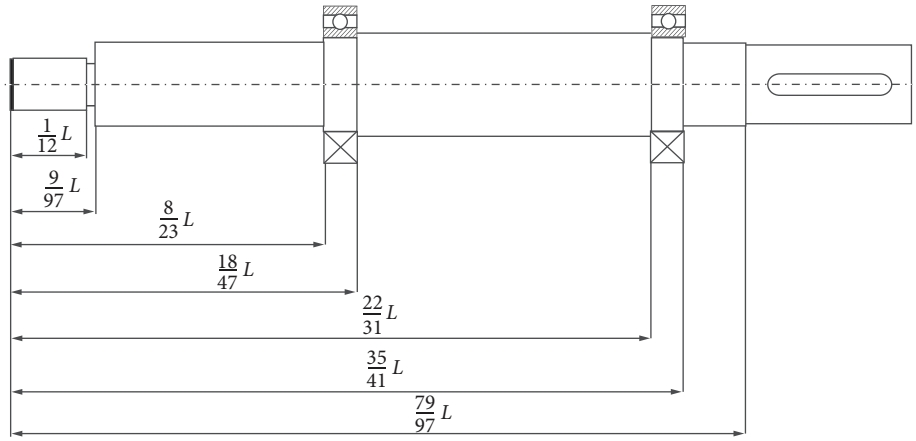

Figure 23: Ratio of each section to total length of the pump shaft.

Table 10: Moment of inertia and β of each section of the pump shaft.

Segment label	Diameter of axle (mm)	Moment of inertia (mm^4)	I_i/I	β_i
I	25	19174.76	1	$1/I$
II	20	7853.982	34/83	$(49/34)(1/I)$
III	40	125663.7	367/56	$-(103/45)(1/I)$
VI	45	201289	21/2	$-(2/35)(1/I)$
V	49	282979	1402/95	$-(2/73)(1/I)$
VI	45	201288.96	21/2	$(2/73)(1/I)$
VII	40	125663.7	367/56	$(2/35)(1/I)$
VIII	38	102353.9	379/71	$(1/29)(1/I)$

According to the different diameters, the shaft is divided into n sections, then the inertia moments of each section are I1, I2, I3 . . .Ii. . .In. I is moment of inertia of pump shaft. Using the step function in the singular function, the reciprocal of the inertia moments of the step shaft of N sections can be expressed as formula (12). β is one of the sub-formulas, which has no specific meaning.

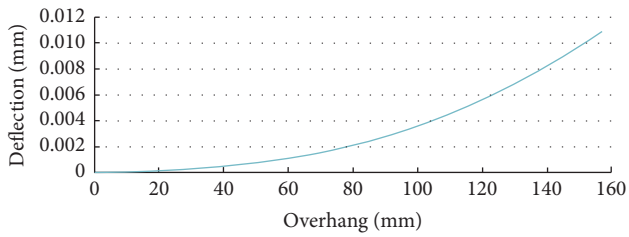

Figure 24: Influence curve of overhang on deflection.

(1) Establishment of Mathematical Model for Optimal Design of Transmission System. The structural dimensions of the pump shaft in this study include eight sections with diameters d_1~d_8 and eight sections with shaft lengths X_1~X_8, as shown in Figure 25. The design basis of the shaft diameter and shaft length of each section of the pump and whether it is necessary to optimize are shown in Table 11. To ensure the smooth transmission of the pump shaft, this study aims at minimizing the deflection of the pump shaft and maximizing the first-order critical speed.

With the minimum deflection as the objective, the objective function is shown:

$$f_1(\vec{X}) = \min y, \quad y = y_1 + y_2, \tag{21}$$

where y is the total displacement of the front end of the pump shaft, y_1 is the total displacement of the extended end of the pump under external force, and y_2 is the total displacement of the pump shaft overhanging the end caused by bearing deformation.

Taking the maximum first-order critical speed as the objective, the objective function is shown:

$$f_2(\vec{X}) = \max n_k, \quad n_k = \frac{60 \times \sqrt{K/m}}{2\pi}. \tag{22}$$

As shown in Figure 17 and Table 9, the relationship between the pump shaft overhang A and the pump shaft span L and the shaft length of each section of the pump shaft is shown in formulas (23) and (24), so the optimization of overhang and span is essentially the optimal value corresponding to each section of the shaft:

$$a = X_1 + X_2 + X_3 + \frac{1}{2}X_4, \tag{23}$$

$$L = X_5 + \frac{X_4}{2} + \frac{X_6}{2}. \tag{24}$$

In this study, the pump shaft is a solid shaft with two supports, so overhang A, span L, clearance c_1 of the front bearing, and clearance c_2 of the rear bearing are taken as design variables, that is,

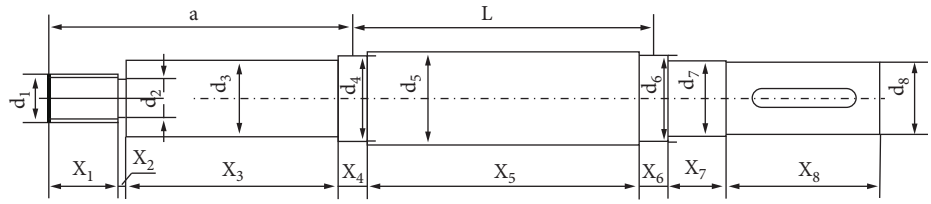

Figure 25: Schematic diagram of structural dimensions of the pump shaft.

Table 11: Structure and dimension of the pump shaft.

Size code	Design basis	Can it be optimized?
d_1	Match with impeller threaded hole	N
d_2	Greater than the minimum design diameter of the pump shaft, according to the standard of relief groove	N
d_3	Select the diameter reference shaft seal	N
d_4	Refer to the bearing inner ring size	N
d_5	2~4 mm larger than the bearing inner ring hole size	N
d_6	Refer to the bearing inner ring size	N
d_7	Refer to the dimensions of the through cover and sealing ring	N
d_8	Cooperate with coupling	N
X_1	The sum of X_1 and X_2 is the depth of the impeller thread hole	N
X_2	According to the relief groove	N
X_3	Greater than shaft seal length	Y
X_4	Less than 1 mm of the bearing width	N
X_5	According to the cantilever length equal to the support span	Y
X_6	Less than 1 mm of the bearing width	N
X_7	Greater than the thickness of the through cover	Y
X_8	Cooperate with the coupling	N

Table 12: Parameter table of NSGA-II algorithm.

Parameter name	Value
Optimal individual coefficient	0.3
Population size	100
Maximum evolutionary algebra	200
Stop algebra	200
Fitness function deviation	1×10^{-100}

$$\vec{X} = [\, a \;\; L \;\; c_1 \;\; c_2 \,]. \tag{25}$$

In the design of the pump shaft, a shaft seal is usually added to the X_3 shaft section to ensure the tightness of the pump shaft transmission. In this study, the M2N mechanical shaft seal made by the Shanghai BURGMANN Company is adopted, and its axial dimension after installation is 58 mm. In addition, considering that the shaft seal needs to have a certain installation space, the minimum size of X_3 is 118 mm. The minimum theoretical size of the span is that the center-to-center distance of two bearings is 16 mm. The maximum dimensions of overhang a and span L refer to the dimensions designed by the pump shaft according to the requirements of a: $L = 1:1$ in the empirical design method; that is, $a = 157.5$ mm and $L = 156$ mm. To sum up, the constraint conditions of pump shaft optimization are as follows (26)–(29):

$$118 \le a \le 157.5, \tag{26}$$

$$16 \le L \le 156, \tag{27}$$

$$-24.39 \le c_1 \le -3.39, \tag{28}$$

$$-24.39 \le c_2 \le -3.39. \tag{29}$$

(2) Solution of the Model. Nondominated Sorting Genetic Algorithms-II (NSGA-II) is a genetic algorithm based on the concept of Pareto optimality, which is an improvement of the selection regeneration method based on the basic genetic algorithm. The main computational process of NSGA-II is to stratify each individual according to their dominance and nondominance relationships and then perform the selection operation, which makes the algorithm obtain very satisfactory results in multiobjective optimization.

According to the above mathematical model of the pump shaft, the optimal values of the pump shaft span and overhang are obtained from the NSGA-II algorithm. The optimization parameters are set as shown in Table 12 and the Pareto frontier of the optimization results is shown in Figure 26.

According to the Pareto solution set, the optimal design parameters are obtained; that is, overhang $a = 118$ mm and span $L = 156$ mm, and the performance indexes before and after optimization are compared, as shown in Table 13. It can be seen from the table that the optimized results are greatly improved compared with the original scheme, and the optimized results are remarkable.

3.4. Test Results. According to the collected data, when the span-to-span ratio is fixed, the deflection of the cantilever end (the third observation point) not only has the largest amplitude at different observation points but also has significant amplitude changes at different rotating speeds, as

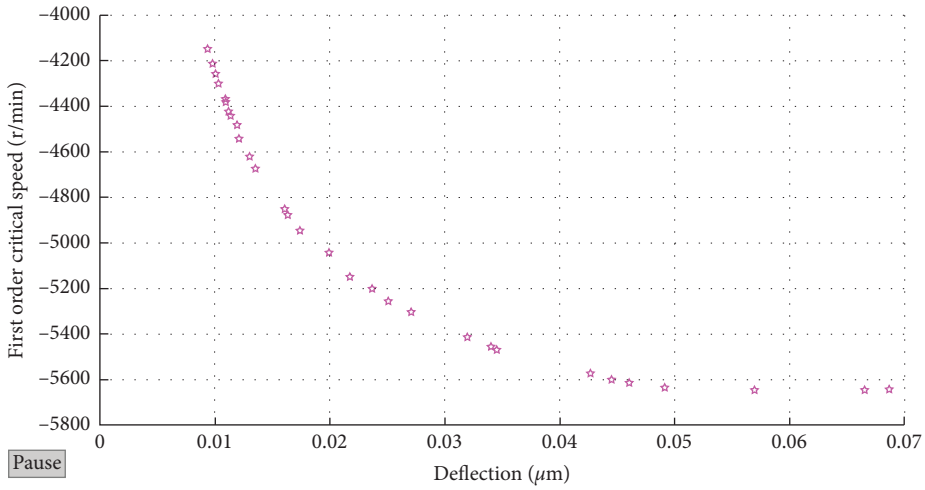

Figure 26: Pareto front end optimization of critical speed and deflection of the pump shaft.

Table 13: Comparison of schemes before and after pump shaft optimization.

Parameter	Initial scheme	Optimum proposal	Improvement effect
Deflection (mm)	0.018616	0.00887	Reduce by 52.35%
Quality (kg)	4.808048	4.415914	Reduce by 8.16%
First order critical speed (r/min)	2906.54	4149.72	Increase by 42.77%

Table 14: Data summary of span-suspension ratio of 1 : 1.

	First observation point	Second observation point	Third observation point
Maximum deflection corresponding speed (r/min)	1100	800	1100
Maximum deflection (μm)	6	2	26
Minimum deflection corresponding speed (r/min)	400	400	400
Minimum deflection (μm)	4	1	5
Year-on-year speed increase (%)	175	100	175
Deflection year-on-year increase (%)	50	100	420

Table 15: Data summary of span-suspension ratio of 1 : 0.75.

	First observation point	Second observation point	Third observation point
Maximum deflection corresponding speed (r/min)	1200	1200	1300
Maximum deflection (μm)	5	2	17
Minimum deflection corresponding speed (r/min)	400	400	400
Minimum deflection (μm)	3	1	5
Year-on-year speed increase (%)	200	200	225
Deflection year-on-year increase (%)	66.67	100	240

Table 16: Data summary of span-suspension ratio of 0.8 : 1.

	First observation point	Second observation point	Third observation point
Maximum deflection corresponding speed (r/min)	1500	400	1000
Maximum deflection (μm)	5	2	27
Minimum deflection corresponding speed (r/min)	400	400	400
Minimum deflection (μm)	3	2	5
Year-on-year speed increase (%)	275	0	150
Deflection year-on-year increase (%)	66.67	0	440

shown in Tables 14–16. In addition, the first observation point is located between the coupling and the front bearing. When comparing different observation points, it can be found that its deflection is usually relatively stable. The second observation point is the middle position of the pump shaft between the two bearings, which reflects the maximum deflection between spans, and the deflection value of the pump shaft is the deformation value of the pump shaft under

the load. To sum up, from the experimental results, it can be concluded that the deflection experimental data with the span-suspension ratio of 1 : 0.75 are the best result among the three groups of experiments, which is consistent with the aforementioned theory.

4. Conclusion

In this study, the influence of the structure of the transmission system on the dynamic performance of a plastic centrifugal pump is studied, and the optimal span cantilever ratio of the pump shaft is verified. The research contents are summarized as follows:

(1) The composition of axial force and radial forces generated by a fluid in a plastic centrifugal pump is analyzed. According to the various structural parameters of the centrifugal pump, the hydraulic model of the impeller and volute is built by Creo5.0, and the axial force and radial force of the fluid were obtained as 324.21 N, and 122.24 N respectively.

(2) After analyzing the mechanical model of the plastic centrifugal pump transmission system, the optimization technology is integrated into the design process. With the singular function as the tool, the minimum deflection of the pump shaft as the objective function, and the structural parameters sensitive to the deflection of the pump shaft as the design variables, the constraint conditions are determined through geometric relations, and the optimization model of the pump transmission system is established. The NSGA-II multiobjective optimization method is used to solve the optimal structural parameters of the optimization model, and the optimal design of the pump shaft span, cantilever, and clearance of front and rear bearings is completed. The optimized result reduces the deflection of the pump shaft by 52.35% and increases the critical speed by 42.77%.

(3) Three groups of cantilever ratios with different spans were collected by the ZT-3 rotor test bed, which were the rotor deflection values of 1 : 1, 1 : 0.75, and 0.8 : 1, respectively. After data comparison, it was verified that the optimal span cantilever ratio of the rotor model with a single-span cantilever structure is 1 : 0.75. Compared with different span cantilever ratios, the rotating speed is increased by 18.18% and 30%, and the deflection is decreased by 34.63% and 37.04%.

Data Availability

The data used to support the findings of this study are included within the article.

Conflicts of Interest

The authors declare that they have no conflicts of interest.

Acknowledgments

This study belongs to the major projects of the "The University Synergy Innovation Program of Anhui Province (GXXT-2019-004)," to the project of the "Teaching Research Project of the Anhui Education Department(2019-jyxm0229)," and "to the project "Science and Technology Planning Project of Wuhu City, 2021YF58."

References

[1] H. Pang, D. Wu, Y. Deng, Q. Cheng, and Y. Liu, "Effect of working medium on the noise and vibration characteristics of water hydraulic axial piston pump," *Applied Acoustics*, vol. 183, Article ID 108277, 2021.

[2] Z. Su, S. Shi, X. Huang, Z. Rao, and H. Hua, "Vibro-acoustic characteristics of a coupled pump-jet-shafting system—SUBOFF model under distributed unsteady hydrodynamics by a pump-jet," *Ocean Engineering*, vol. 17, p. 235, 2021.

[3] W. Li, "Finite element analysis of shaft strength of multistage centrifugal pump based on APDL," *Journal of Agricultural Machinery*, vol. 43, no. 5, pp. 69–73, 2012.

[4] L. Jia, H. Li, W. Wang, and Blair, "Multi-objective optimization design and simulation analysis of fuel centrifugal pump," *Propulsion Technology*, vol. 42, no. 3, 2021.

[5] E. Riccietti, J. Bellucci, M. Checcucci, M. Marconcini, and A. Arnone, "Support vector machine classification applied to the parametric design of centrifugal pumps," *Engineering Optimization*, vol. 50, no. 8, pp. 1304–1324, 2018.

[6] K. H. Wu, B. J. Lin, and C. I. Hung, "Novel design of centrifugal pump impellers using generated machining method and CFD," *Engineering Applications of Computational Fluid Mechanics*, vol. 2, no. 2, pp. 195–207, 2014.

[7] C. Y. Khor, M. A. M. Nawi, M. Ikman Ishak, Z. K. Ooi, M. U. Rosli, and S. N. A. Ahmad Termizi, "Simulation analysis of the thickness effect towards mechanical aspects in the design of centrifugal pump casing," *IOP Conference Series: Materials Science and Engineering*, vol. 864, no. 1, Article ID 012192, 2020.

[8] Y. Xu, L. Tan, S. Cao, and W. Qu, "Multiparameter and multiobjective optimization design of centrifugal pump based on orthogonal method," *Proceedings of the Institution of Mechanical Engineers—Part C: Journal of Mechanical Engineering Science*, vol. 231, no. 14, pp. 2569–2579, 2017.

[9] S. M. Rajmane and S. P. Kallurkar, "Use of CFD tool for improving design of centrifugal pump," *International Journal of Latest Trends in Engineering and Technology*, vol. 7, no. 4, pp. 407–420, 2016.

[10] R. Zhang, L. Gao, and X. Chen, "Optimization design of centrifugal pump impeller based on multi-output Gaussian process regression," *Modern Physics Letters B*, vol. 35, no. 21, Article ID 2150364, 2021.

[11] J. Zhang, L. Ye, S. Yuan, and H. Vilen, "Influence of splitter blades on radial force characteristics of centrifugal pump," *Research on Agricultural Mechanization*, vol. 35, no. 10, pp. 181–185, 2013.

[12] X. Guan, *Modern Pump Theory and Design*, China Aerospace Press, Beijing, China, 2011.
[13] C. Gong, L. Zheng, S. Qian, H. Zhuang, and J. Hu, "Summary of calculation methods of axial force and radial force of dredger mud pump shaft," *China Harbor Construction*, vol. 26, no. 1, pp. 63–67, 2016.
[14] D. Paul, H. Agarwal, and B. R. Ponangi, "CFD analysis of two-phase cavitating flow in a centrifugal pump with an inducer," *Heat Transfer*, vol. 49, no. 6, pp. 3854–3881, 2020.
[15] M.-Z. Li, Y.-P. He, Y.-D. Liu, and C. Huang, "Analysis of transport properties with varying parameters of slurry in horizontal pipeline using ANSYS fluent," *Particulate Science and Technology*, vol. 38, no. 6, pp. 726–739, 2020.